Journal of *Marine Science and Engineering*

MDPI

Article

Research on Decoupling Duty Cycle Optimization Control Method of a Multiport Converter for Dual-Port Direct Drive Wave Power Generation System

Lei Huang *, Shixiang Wang, Baoyi Pan, Haitao Liu, Jiyu Zhang and Shiquan Wu

School of Electrical Engineering, Southeast University, Nanjing 210096, China; wangshixiang@seu.edu.cn (S.W.); 220232860@seu.edu.cn (B.P.); 220213149@seu.edu.cn (H.L.); 230229410@seu.edu.cn (J.Z.); 220222725@seu.edu.cn (S.W.)

* Correspondence: huanglei@seu.edu.cn

Abstract: Dual-port direct drive wave energy power generation systems (DP-DDWEPGS) have received widespread attention due to their smooth and zero-free output power, compared to single-port direct drive wave energy power generation systems (SP-DDWEPGS) which have the disadvantage of large out-put power fluctuations. To further enhance the performance of the DP-DDWEPGS, optimal power capture control is proposed to achieve maximum power point tracking. Meanwhile, a multiport converter is applied to the DP-DDWEPGS to solve the problem caused by an excessive number of switching devices in the overall system converter. The multiport converter fulfills all the functional requirements of the DP-DDWEPGS while reducing the number of switching devices. However, switch multiplexing of the multiport converter also introduces coupling relationships between each port and the wave force exhibits time-varying characteristics, necessitating advanced control methods with superior fast-tracking capability. Therefore, in this paper, a decoupling duty cycle optimization model predictive control for DP-DDWEPGS is proposed. Based on the characteristics of switching multiplexing, NSC finite control set model predictive control (FCS-MPC) decouples the current prediction and the cost function, reduces the number of candidate voltage vectors in each operation, and shortens the operation time by 70%. To address the issues of high ripple value and increased error due to decoupling in FCS-MPC, duty cycle optimization control is added, greatly reducing the fluctuations in electromagnetic force and power of the permanent magnet linear generator (PMLG). Based on the established simulation model, the feasibility and superiority of the multiport converter and decoupling duty cycle optimization model predictive current control method are verified.

Keywords: dual-port direct drive wave energy power generation systems (DP-DDWEPGS); optimal power capture control; decoupling duty cycle optimization model predictive current control (MPCC-DD); nine-switch converter (NSC); hybrid energy storage system (HESS); permanent magnet linear generator (PMLG)

Citation: Huang, L.; Wang, S.; Pan, B.; Liu, H.; Zhang, J.; Wu, S. Research on Decoupling Duty Cycle Optimization Control Method of a Multiport Converter for Dual-Port Direct Drive Wave Power Generation System. *J. Mar. Sci. Eng.* **2024**, *12*, 1811. https://doi.org/10.3390/jmse12101811

Academic Editors: Pedro Beirão and Mário J. G. C. Mendes

Received: 23 September 2024
Revised: 7 October 2024
Accepted: 8 October 2024
Published: 11 October 2024

1. Introduction

Direct drive wave energy power generation systems (DDWEPGS) exhibit high energy conversion efficiency due to the elimination of gearboxes, hydraulic equipment and air compressor, compared with non-direct wave energy converters [1,2]. The DDWEPGS mainly consists of two configurations: the single-port direct drive wave energy power generation system (SP-DDWEPGS) and the dual-port direct drive wave energy power generation system (DP-DDWEPGS). The SP-DDWEPGS has only one power output port, whereas the DP-DDWEPGS is equipped with dual power output ports as shown in Figure 1 [3]. Under the driving of a wave, the velocity of the floats exhibits a periodic variation. As the float of the DP-DDWEPGS directly drives the translator of the linear permanent magnet generator (PMLG), the output power of the PMLG also varies in periodic fluctuation [4]. By adjusting the translators' electromagnetic force, the DP-DDWEPGS can achieve two

complementary output powers, resulting in a total output power that is smooth and free of zero-crossings [5]. This feature makes the performance of the DP-DDWEPGS superior to that of the SP-DDWEPGS. But it is worth noting that DP-DDWEPGS employs a dual-electrical-ports dual-mechanical-ports machine system. This results in differences in the system dynamics and equivalent circuit compared to SP-DDWEPGS. Consequently, DP-DDWEPGS has a unique optimal power capture strategy that has not been extensively studied in previous literature.

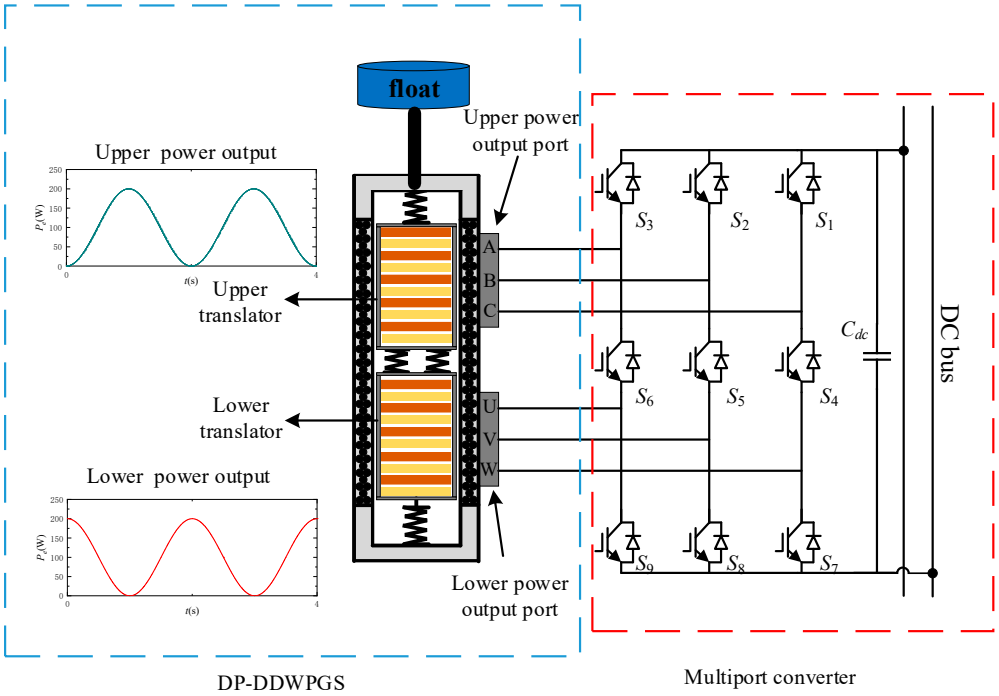

Figure 1. DP-DDWEPGS with multiport converter.

Meanwhile, the dual power outputs of the DP-DDWEPGS require two discrete three-phase voltage source rectifiers (VSRs). Due to the fluctuating nature of wave energy conversion, DP-DDWEPGS must be coupled with a hybrid energy storage system (HESS) through two sets of DC-DC converters. These converters result in an excessive number of switching devices in the overall system. This configuration leads to a higher failure rate, poor stability, and increased costs. To address these issues, the multiport converter was proposed to reduce the number of switching devices in the converter by sharing the switching legs, which provides excellent application prospects [6].

As a typical multiport converter, the nine-switch converter (NSC) features two AC ports and one DC port, as shown in Figure 1. The three ports of the NSC are derived by switch multiplexing two three-phase voltage source rectifiers (VSRs). While maintaining the full functions of VSRs, the NSC reduces the number of switching devices by 25% [7,8]. However, the control method of the NSC differs from that of the VSRs. Switch multiplexing introduces coupling relationships between the ports of the NSC, preventing the independent and free control of each port as is possible with VSRs [9–11]. Additionally, conventional linear controllers require different modulation strategies for the NSC under common-frequency and difference-frequency modes. This makes the conventional control methods for the NSC particularly complex, and it is difficult to achieve fast tracking with the linear controller in a nonlinear environment [12]. To address the issue, finite control set model predictive control (FCS-MPC) is applied to the NSC. FCS-MPC considers the voltage vectors corresponding to the switching states of the switching devices as a finite control set. In each calculation, it uses all the voltage vectors in the control set to predict the system behavior for the next state, then selects the switching state that can minimize the desired cost function. Compared to linear controllers, FCS-MPC is advantageous due to its

fast response in dynamic processes, elimination of the need for a pulse width modulator, and its ability to easily incorporate nonlinearities and NSC system constraints [13]. The determination of the switching states in the finite control set of FCS-MPC has a significant impact on the overall control performance [14]. The NSC has a total of 27 switching states, as shown in Table A1 in Appendix A. Gao et al. [15] calculate the 27 switching states of NSC and sum the cost functions of the dual ports into a single overall cost function. However, calculating 27 switching states per operation imposes a significant burden on the microcontroller. Although there are 27 possible switching states for the NSC, some of these states are redundant. It is found that only 15 switching states are sufficient to control the dual AC loads independently. These 15 switching states are considered a finite solution set of predictive control schemes to minimize computation [16]. Furthermore, a dual predictive current control for NSC was proposed to separate the control of the induction generator from the grid control [17]. The two controllers operate alternately and independently to decouple the cost function. The finite control set contains only eight candidate voltage vectors, significantly reducing the computational burden, with extremely fast computational speed.

However, it is worth noting that the standard FCS-MPC applies only one voltage vector in each control cycle, resulting in a high ripple in the steady state [18]. To address this issue, an improved model predictive direct power control is proposed for a pulse width modulation rectifier by using a duty cycle control [19]. This approach introduces the concept of duty cycle control by allocating the operating time between non-zero voltage vectors and zero vectors within the control cycle. The non-zero vectors and their operating time are selected based on the principle of minimizing the effect of the non-zero vectors and the power error. In direct torque control, to reduce torque and flux ripples, a finite control set of new candidate voltage vectors with different duty cycles is synthesized by inserting zero vectors along the optimal voltage vectors [20].

Additionally, due to the volatility of the wave, the HESS is commonly used with DDWEPGS [21,22]. However, HESS connected to the DC bus through bidirectional DC-DC converters, which results in the redundancy of switching devices, high failure rate, and power multilevel flow [23]. An integrated dual-input DC-DC converter is proposed to address this problem, but it lacks research on power bidirectional flow [24].

In this paper, an equivalent circuit diagram of DP-DDWEPGS is established by hydrodynamic analysis. Based on the equivalent circuit diagram, optimal power capture control is proposed to achieve maximum power point tracking for DP-DDWEPGS. Meanwhile, a multiport converter is proposed to address the issues of high fault rates, high costs, and low stability caused by the excessive number of switching devices in DP-DDWEPGS. This multiport converter is derived by switch multiplexing two three-phase VSRs and two DC-DC converters and can perform all the functions of these converters while reducing the number of switching devices by 25%. However, the coupling relationships and constraints between the ports of the multiport converter make the design of linear controllers complex. The time-varying wave speed and displacement lead to time-varying electromagnetic forces in the generator, necessitating rapid control response. FCS-MPC is employed to meet these requirements. Furthermore, decoupling model predictive current control (MPCC-D) is proposed to decouple NSC dual ports and the cost function. As a result, the computational load is reduced by 80%, significantly speeding up the calculations. However, since MPCC-D applies a single voltage vector only once per control cycle and each control cycle activates only one port, it results in high ripple and increased fluctuations in steady state. Duty cycle optimization control is proposed to address this issue, allocating the operating time between optimal voltage vectors and zero voltage vectors in each control cycle, which greatly reduces ripple and fluctuations.

This paper is organized as follows: Section 2 details the optimal power capture analysis of the DP-DDWEPGS. Section 3 describes in detail the mathematical model analysis of DP-DDWEPGS. Section 4 provides an in-depth study of the improved FCS-MPC combining decoupling and duty cycle control. Section 5 verifies the feasibility of the proposed control

strategy multi-port converter through simulation. Finally, the paper is summarized in Section 6.

2. Optimal Power Capture Analysis of the DP-DDWEPGS

The proposed DP-DDWEPGS consists of dual translators connected by the spring and a float rigidly connected to the upper translator. By analyzing the forces between them, the maximum power point can be obtained.

2.1. Hydrodynamic Model of Float

The decomposition of the forces acting on the float is shown in Figure 2. The hydrodynamic equations are as follows [1]:

$$m_b\ddot{x}(t) = F_{ex}(t) + F_{rad}(t) + F_h(t) - F_{line}(t) \tag{1}$$

where $x(t)$ is the float swing displacement with respect to the horizontal plane, m_b is the float mass, $F_{ex}(t)$ is the wave excitation force, $F_{rad}(t)$ is the radiation force, $F_h(t)$ is hydrostatic resilience, $F_{line}(t)$ is the rope force connecting the float to the power take off (PTO) device.

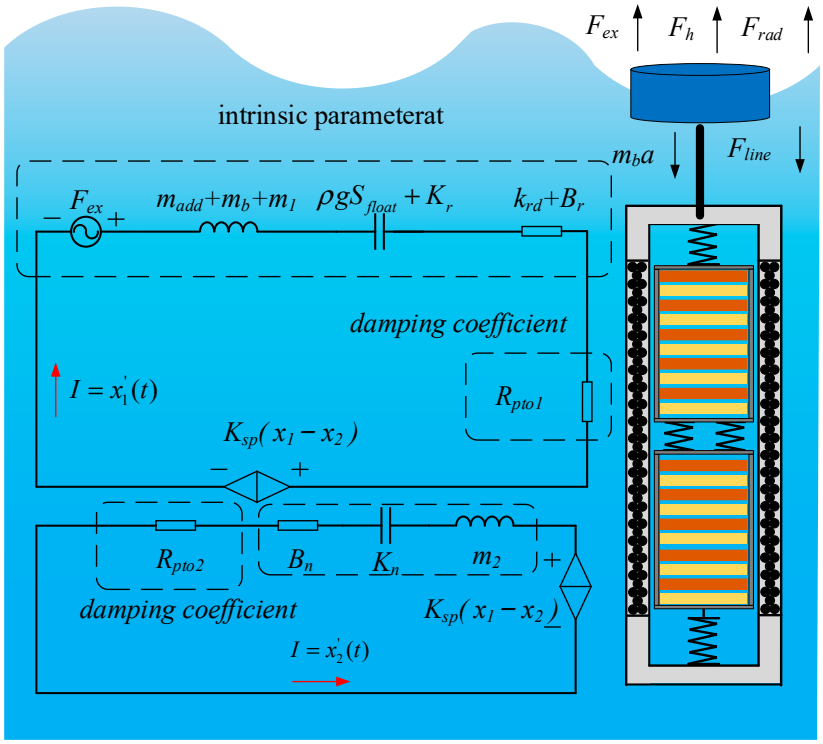

Figure 2. Equivalent circuit diagram of DP-DDWEPGS.

$F_{rad}(t)$ consists of two components, acceleration and velocity, and can be expressed in regular wave changes as

$$F_{rad}(t) = -k_{rd}\dot{x}(t) - m_{add}\ddot{x}(t) \tag{2}$$

where k_{rd} is the radiative damping and m_{add} is the added mass.

$F_h(t)$ can be obtained from the buoyancy equation

$$F_h(t) = -\rho g S_{float} x(t) \tag{3}$$

where ρ is the density of seawater, g is the acceleration of gravity, and S_{float} is the buoyant area of the float.

The hydrodynamic equilibrium equation can be obtained by bringing Equations (2) and (3) into Equation (1)

$$(m_{add} + m_b)\ddot{x}(t) + k_{rd}\dot{x}(t) + \rho g S_{float} x(t) = F_{ex}(t) - F_{line}(t) \tag{4}$$

2.2. Optimal Power Capture of DP-DDWEPGS

Decoupling the force on the float from the force on the PTO device leads to the force equation of the dual-translator

$$\begin{cases} m_1\ddot{x}_1(t) = F_{line}(t) - k_{sp}(x_1(t) - x_2(t)) - F_{em1}(t) - B_r\dot{x}_1(t) - K_r x_1(t) \\ m_2\ddot{x}_2(t) = k_{sp}(x_1(t) - x_2(t)) - F_{em2}(t) - B_n\dot{x}_2(t) - K_n x_2(t) \end{cases} \tag{5}$$

where m_1 and m_2 are the masses of the upper and lower translator, k_{sp} is the spring coefficient, $x_1(t)$and $x_2(t)$ are the dual translator displacements, $F_{em1}(t)$ and $F_{em2}(t)$ are the dual translator electromagnetic forces, K_r and B_r are the spring coefficient and elastic damping of the up end-stop spring, K_n and B_n are the spring coefficient and elastic damping of the restoring-spring.

When the PMLG moves coaxially with the PTO device, without considering the motion offset of the translator with respect to the device, in order to maximize the active power emitted by the PMLG, the electromagnetic force and velocity need to be kept in-phase in order to reduce the generation of reactive power [1], and hence the following can be obtained:

$$\begin{cases} F_{em1}(t) = R_{pto1}\dot{x}_1(t) \\ F_{em2}(t) = R_{pto2}\dot{x}_2(t) \end{cases} \tag{6}$$

where R_{pto1} and R_{pto1} are the damping coefficients of the upper translator and the lower translator.

From Equations (4) and (5), considering the upper translator is rigidly connected to the float, $x(\omega) = x_1(\omega)$, $\dot{x}(\omega) = \dot{x}_1(\omega)$, an equivalent circuit diagram can be obtained as shown in Figure 2, considering $m_{add} + m_b + m_1$ and m_2 as inductance values, $k_{rd} + B_r$ and B_n as resistance values, and $\rho g S_{float} + K_r$ and K_n as capacitance values. These parameters are referred to as the intrinsic parameters of the wave power generator. $k_{sp}(x_1 - x_2)$ is considered as a controlled voltage source. The velocity of the float is then equivalent to the current in the first circuit of Figure 2, and the velocity of the lower translator is equivalent to the current in the second circuit with a controlled voltage source of Figure 2.

Bringing (6) into Equation (5) and performing the Laplace transform, then converting to the frequency domain yields:

$$\frac{x_1(\omega)}{x_2(\omega)} = \frac{k_{sp} - \omega^2 m_2 + j\omega(R_{pto2} + B_n) + K_n}{k_{sp}} \tag{7}$$

In DP-DDWEPGS, the velocity phase difference between the dual translators is $\pi/2$, which leads to the following equation:

$$k_{sp} + K_n = \omega^2 m_2 \tag{8}$$

The total output power of DP-DDWEPGS is the sum of the output power of the dual translators, in order to ensure the stability of the total instantaneous power and reduce the power superposition fluctuations, the ideal output power of the dual translators should have the same amplitude, which can be obtained from the following conditions:

$$F_{em1}(\omega)x_1'(\omega) = F_{em2}(\omega)x_2'(\omega) = \frac{1}{2}P_{pto} \tag{9}$$

Let $x_1'(\omega) = \lambda x_2'(\omega)$, at a single frequency, λ is a constant.

Performing the Laplace transform transforms Equations (4) and (5) into the frequency domain, combining with $x(\omega) = x_1(\omega)$, $x'(\omega) = x'_1(\omega)$ and $\lambda = x_1'(\omega)/x_2'(\omega)$ gives

$$\begin{cases} F_{ex}(\omega) = j\omega(m_{add} + m_b + m_1)x'(\omega) + (k_{rd} + B_r)x'(\omega) \\ \quad +(\rho g S_{float} + K_r)\frac{x'(\omega)}{j\omega} + F_{em1} + k_{sp}(x_1(\omega) - x_2(\omega)) \\ k_{sp}(x_1(\omega) - x_2(\omega)) = j\omega m_2 x_2'(\omega) + F_{em2} + B_n x_2'(\omega) + K_n\frac{x_2'(\omega)}{j\omega} \end{cases} \tag{10}$$

Combining the two formulas in Equation (10) and bringing in $\lambda = x_1'(\omega)/x_2'(\omega)$ yields

$$\begin{aligned} F_{ex}(\omega) &= j\omega(m_{add} + m_b + m_1 + \tfrac{m_2}{\lambda})x'(\omega) + (k_{rd} + B_r + \tfrac{B_n}{\lambda})x'(\omega) \\ &\quad +(\rho g S_{float} + K_r + \tfrac{K_n}{\lambda})\tfrac{x'(\omega)}{j\omega} + (1+\lambda)R_{pto1}x'(\omega) \end{aligned} \tag{11}$$

The principle of analog circuits can be employed to determine the optimal R_{pto}. In Equation (11), the upper translator velocity $x'(\omega)$ is used as the current and the excitation force $F_{ex}(\omega)$ is used as the voltage, and the damping coefficient $(1 + \lambda)R_{pto1}$ is used as the resistance value. To achieve the maximum power from waves for the DP-DDWEPGS, the damping coefficient of the generator is equal to the modulus of the intrinsic parameter of the wave power generator, and the damping coefficient is

$$\begin{cases} (1+\lambda)R_{pto1} = \sqrt{\left[\omega(m_{add} + m_b + m_1 + \frac{m_2}{\lambda}) - \frac{1}{\omega}(\rho g S_{float} + K_r + \frac{K_n}{\lambda})\right]^2 + (k_{rd} + B_r + \frac{B_n}{\lambda})^2} \\ R_{pto2} = \lambda^2 R_{pto1} \end{cases} \tag{12}$$

3. Mathematical Model Analysis of DP-DDWEPGS

The proposed multiport converter applied to DP-DDWEPGS consists of a nine-switch converter (NSC) and an integrated DC-DC converter, and its topology and control block diagram are shown in Figure 3. NSC is interfaced with a dual-port permanent magnet linear generator (DP-PMLG), functioning as a rectifier. Concurrently, an integrated bidirectional DC-DC converter facilitates the connection between the DC bus and the HESS to maintain power stability on the load side.

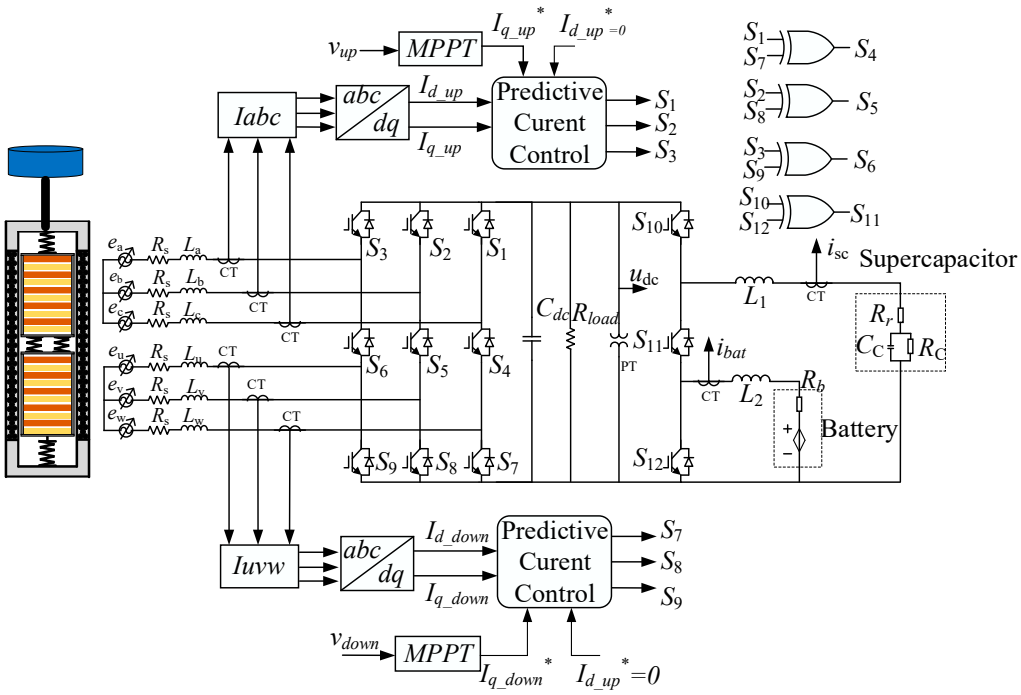

Figure 3. Topology and control block diagram of proposed multiport converter.

3.1. Mathematical Modeling of DP-DDWEPGS' Generator Side

The nine-switch converter configuration is derived from the back-to-back converter through switch multiplexing. In this arrangement, each of the AC terminals is linked to either $+V_{dc}$ or ground, necessitating two switches to be active and one switch to be inactive in each leg of the converter. This constraint yields three distinct switching states per leg, amounting to a total of 27 switching states, as elaborated in Table A1.

Dual translators of the PMLG in DPDDWEPGS have identical parameters; therefore, only one port needs to be analyzed. According to the generator convention, the voltage equation of PMLG in the d/q coordinate system, which is based on mover magnetic field orientation, can be obtained as follows [25]

$$\begin{cases} u_d = -R_s i_d - L_d \frac{di_d}{dt} + \frac{\pi v}{\tau} L_q i_q \\ u_q = \frac{\pi v}{\tau} \psi_f - R_s i_q - L_q \frac{di_q}{dt} - \frac{\pi v}{\tau} L_d i_d \end{cases} \tag{13}$$

where u_d, i_d is the voltage and current of the d-axis equivalent winding, u_q, i_q is the voltage and current of the q-axis equivalent winding, L_d, L_q is the inductance of the d-axis and q-axis equivalent windings, τ is pole pitch of PMLG, and ψ_f is the flux-linkage of the permanent magnet.

The active power can be expressed as

$$P_{em} = \frac{3\pi v}{2\tau}(\psi_f i_q + (L_d - L_q) i_d i_q) \tag{14}$$

If $i_d = 0$ control strategy is used, the electromagnetic force of PMLG can be expressed as

$$F_{em} = R_{PTO} v = \frac{P_{em}}{v} = \frac{3\pi}{2\tau} \psi_f i_q \tag{15}$$

Conventional model predictive current control (MPCC) for the derivative phase of electron current, discretized using the Eulerian approximation

$$\frac{di}{dt} \approx \frac{i(k+1) - i(k)}{T_s} \tag{16}$$

According to Equations (13) and (16), d/q axis predictive current can be expressed as

$$\begin{cases} i_d(k+1) = (1 - T_s \frac{R_s}{L_d}) i_d(k) + T_s \frac{\pi v(k)}{\tau} \frac{L_q}{L_d} i_q(k) - T_s \frac{u_d(k)}{L_d} \\ i_q(k+1) = (1 - T_s \frac{R_s}{L_d}) i_q(k) + T_s \frac{\pi v(k)}{\tau L_q} \psi_f - T_s \frac{\pi v}{\tau} \frac{L_d}{L_q} i_d(k) - T_s \frac{u_q(k)}{L_q} \end{cases} \tag{17}$$

The MPCC for dual translators is consistent in both Equation (17), and the cost function. The $i_d = 0$ control strategy is implemented in this system, and the q axis current is controlled to achieve target damping. The cost function is used to realize the fast following of the actual current to the reference value of d/q axis current. Therefore, the cost function of the upper translator and lower translator are expressed as

$$\begin{cases} g_{up\_j} = (i^*_{d\_up}(k+1) - i_{d\_up}(k+1))^2 + (i^*_{q\_up}(k+1) - i_{q\_up}(k+1))^2 \\ g_{down\_j} = (i^*_{d\_down}(k+1) - i_{d\_down}(k+1))^2 + (i^*_{q\_down}(k+1) - i_{q\_down}(k+1))^2 \end{cases} \tag{18}$$

where g_{up_j} is the cost function of the upper translator, and g_{down_j} is the cost function of the lower translator. The reference value of i_q at MPPT (maximum power point tracking) can be obtained from Equations (6), (12), and (15)

$$\begin{cases} i^*_{q\_up}(k+1) = \frac{2\tau}{3\pi\psi_f} R_{pto1} v_1(k) \\ i^*_{q\_down}(k+1) = \frac{2\tau}{3\pi\psi_f} R_{pto2} v_2(k) \end{cases} \tag{19}$$

Considering the upper translator and lower translator have an equal effect [15], the total cost function is written as

$$J = g_{up\_j} + g_{down\_j} \tag{20}$$

3.2. Mathematical Modeling of DP-DDWEPGS' Hybrid Energy Storage System Side

The integrated bidirectional DC-DC converter is achieved through switch multiplexing, like the nine-switch converter. However, it differs in that all three of its ports are DC-powered. In this study, a HESS comprising supercapacitors and batteries is employed to mitigate system power fluctuations. The supercapacitor handles high-frequency power fluctuations, while the battery addresses low-frequency variations. This configuration offers benefits such as rapid response, prolonged service life, and cost-effectiveness.

In addressing wave power fluctuations, the equilibrium of power required to stabilize the total power within the DC link is delineated into two distinct components [26]: (1) average power component P_{avg} and (2) transient power component P_{tran}. The power balance equation can be articulated as follows:

$$P_{load} - P_g = P_{sc} + P_{bat} = P_{tran} + P_{avg} \tag{21}$$

where P_{load} is the load power and P_g is the generator power, the requisite net power to stabilize the DC bus voltage within a designated range can be expressed as follows:

$$P_{tran} + P_{avg} = i_{tot} u_{dc} \tag{22}$$

where i_{tot} denotes the total current, u_{dc} is the busbar voltage, it is acknowledged that i_{tot} comprises a transient current component i_{tran}, and an average current component i_{avg}, with i_{tran} being the reference current for the supercapacitor and i_{avg} being the reference amount for the battery current. Their reference values can be obtained as

$$\begin{cases} i_{bat}^*(s) = i_{avg}(s) = \frac{\omega_c}{s+\omega_c} i_{tot}(s) \\ i_{sc}^*(s) = i_{tran}(s) = i_{tot}(s) - i_{avg}(s) \end{cases} \tag{23}$$

where ω_c is the cutoff frequency of the LPF.

4. Decoupling Duty Cycle Optimization Model Predictive Control

4.1. Model Predictive Control of NSC

The voltage vector model of the NSC forms the basis for the current model prediction and cost function evaluation steps. In this context, NSC for DP-DDWEPGS, with its 27 voltage vectors, is utilized, as shown in Table A1. The cost function, which encompasses all variables of the dual-port system, is predicted using a conventional current model. We refer to this type of control as MPCC, and its control algorithm is shown in Figure 4.

The algorithm to derive the optimal voltage vector requires 27 calculations, shown in Table A1, which poses a computationally intensive task for an embedded system. Additionally, the algorithm centralizes the variables of the upper and lower ports into a single cost function. This approach results in a cost function that is dominated by the port with the higher current difference, consequently ignoring the port with the lower current difference.

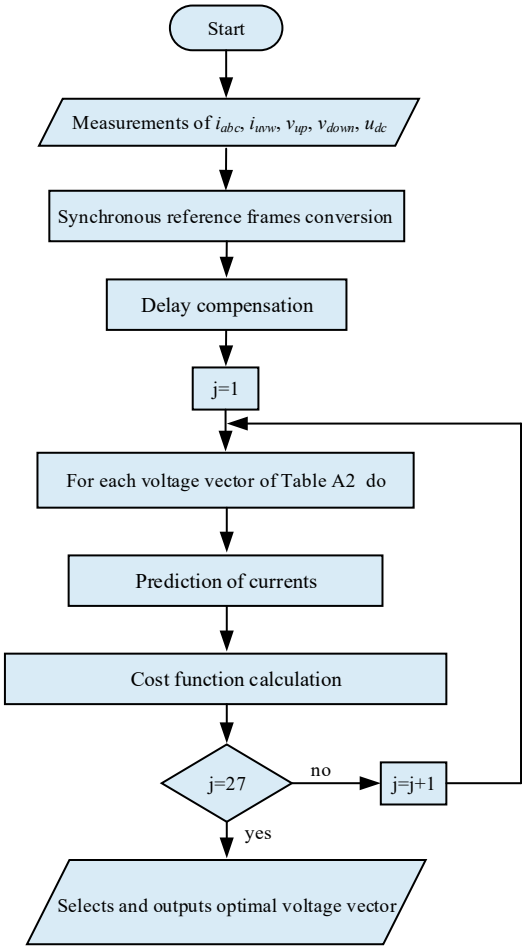

Figure 4. Flowchart of overall control algorithm of MPCC.

4.2. Decoupling MPCC

NSC is derived from the back-to-back converter through switch-multiplexing, which allows the NSC to function as a dual-port converter while maintaining the same control strategy as the back-to-back converter. This is achieved through the decoupling strategy proposed in this paper (MPCC-D). The decoupling strategy is outlined as follows: when the lower three switches are all on, the upper port operates as a three-phase VSR, referred to as state A, as shown in Figure 5a. Conversely, when the upper three switches are all on, the lower port operates as a three-phase VSR, referred to as state B, as shown in Figure 5b.

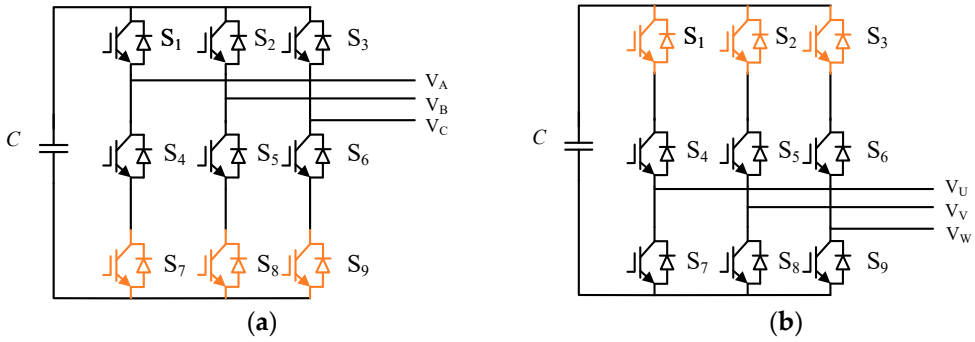

Figure 5. Decoupling strategy. (**a**) State A ([S_7, S_8, S_9] = [1, 1, 1]); (**b**) State B ([S_1, S_2, S_3] = [1, 1, 1]).

In state A, the upper port three-phase VSR has only eight voltage vectors (V_0~V_7 shown in Table A1), and in state B, the lower port three-phase VSR also has only eight voltage vectors (V_0~V_7). Decoupling of the upper and lower port MPCC is achieved when

the upper and lower port MPCC are operated alternately, with each MPCC operating at half the discretization time, as shown in Figure 6. At this time, the cost function also realizes decoupling and is divided into two parts corresponding to each port (24).

$$\begin{cases} J_{stateA} = g_{up\_j} \\ J_{stateB} = g_{down\_j} \end{cases} \tag{24}$$

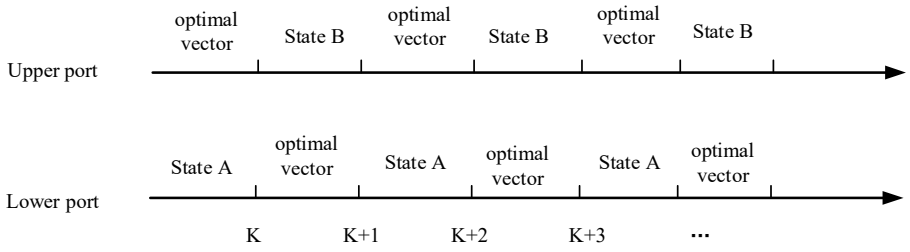

Figure 6. Port operation timing in discrete time.

After the decoupling of the dual ports of the NSC and cost function, the optimal voltage vector can be obtained with only eight calculations, greatly reducing the computation time. At the same time, since states A and B are composed of zero vectors [1, 1, 1], each port inserts zero vectors between the optimal voltage vectors, creating a time gap. This process eliminates the delay from the prediction stage, making the delay compensation link unnecessary.

4.3. Duty Cycle Optimization of Decoupling MPCC

To reduce ripple and fluctuations in maximum power point tracking and electromotive force, decoupling duty cycle optimization model predictive current control (MPCC-DD) is proposed in this paper. This method targets the given value of i_q from Equation (20) and, by adjusting the action time of the optimal voltage vector and the zero vector, ensures that the actual value of i_q is exactly equal to its given value before the end of the next control cycle. Figure 7 shows the schematic diagram of the dead beat.

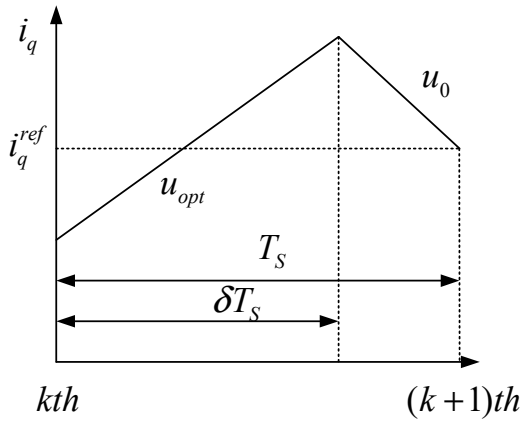

Figure 7. Schematic diagram of dead beat.

From Figure 7, it can be seen that the optimal voltage vector u_{opt} combined with the zero vector u_0 acts in the same control cycle. The predicted value of i_q at the moment of $(k + 1)$ is equal to the given value of i_q from MPPT. δ is the duty cycle of u_{opt}.

Derivation of Equation (13) with respect to time yields

$$\frac{di_q}{dt} = \frac{-u_q + \omega_r \psi_f - R_s i_q}{L_q} - \omega_r i_d \tag{25}$$

According to Equation (25), the slope of i_q after the action of different voltage vectors can be obtained as follows:

$$\begin{cases} S_0 = \frac{di_q}{dt}\Big|_{u_q=0} = \frac{\omega_r\psi_f - R_s i_q}{L_q} - \omega_r i_d \\ S_{opt} = \frac{di_q}{dt}\Big|_{u_q=u_{opt}} = \frac{\omega_r\psi_f - R_s i_q}{L_q} - \omega_r i_d - \frac{u_q}{L_q} \end{cases} \tag{26}$$

where S_0 denotes the i_q slope corresponding to the zero vector, and S_{opt} denotes the i_q slope corresponding to the optimal voltage vector.

Making the value of i_q at the next moment equal to the given value of i_q^{ref}, the equation for i_q is given by

$$i_q(k+1) = i_q^{ref} = i_q(k) + S_{opt}\delta T_s + S_0(1-\delta)T_s \tag{27}$$

The optimal vector duty cycle can be obtained

$$\delta = \frac{i_q^{ref} - i_q(k) - S_0 T_s}{(S_{opt} - S_0)T_s} = \frac{i_q^{ref} - i_q(k) - T_s(\frac{\omega_r\psi_f - R_s i_q(k)}{L_q} - \omega_r i_q(k))}{(-\frac{u_q(k)}{L_q})T_s} \tag{28}$$

Since the parameters of the dual translator are the same, except for the different i_q^{ref}, the other control modes are exactly the same, and the specific control diagram is shown in Figure 8.

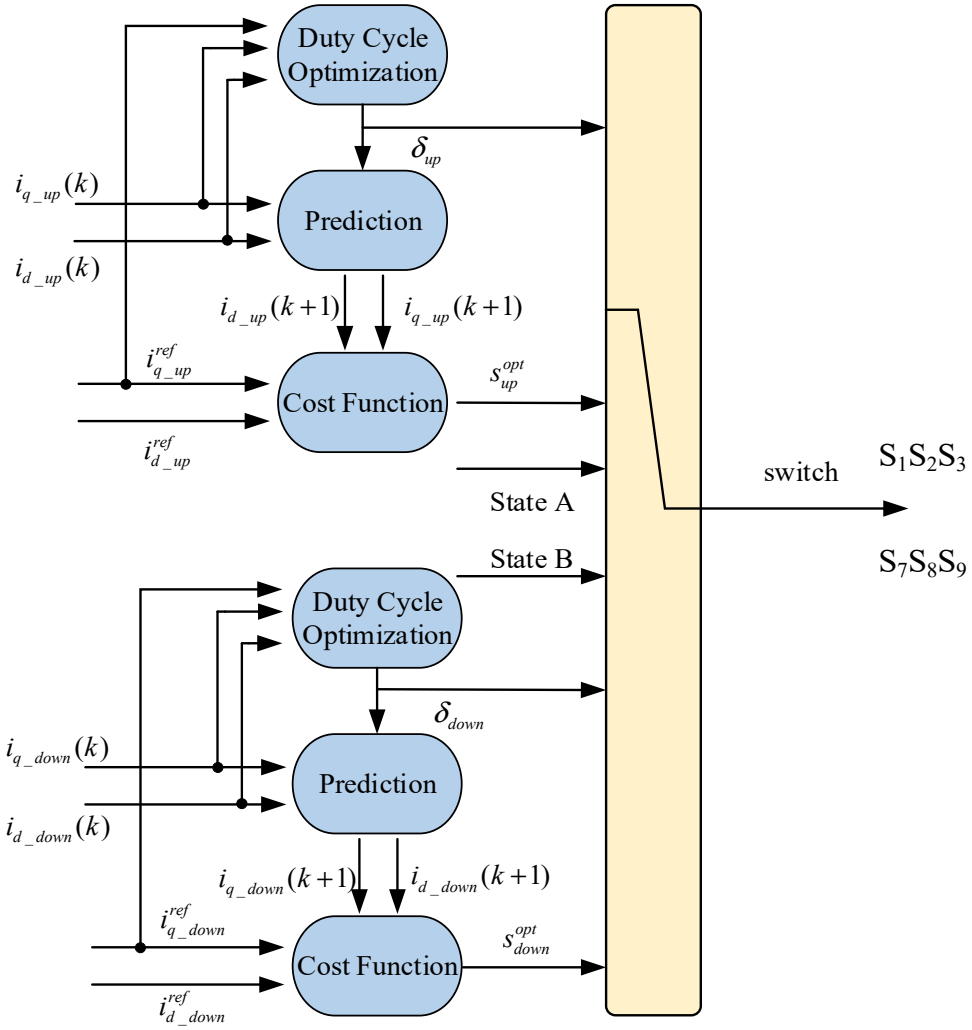

Figure 8. Specific control diagram of MPCC-DD.

The MPCC of the NSC dual ports is alternated and the duty cycle optimization calculation is added so that the acting voltage vector and zero vector work together to reduce the maximum power point fluctuation. We refer to this type of control as MPCC-DD, and its overall control algorithm is shown in Figure 9.

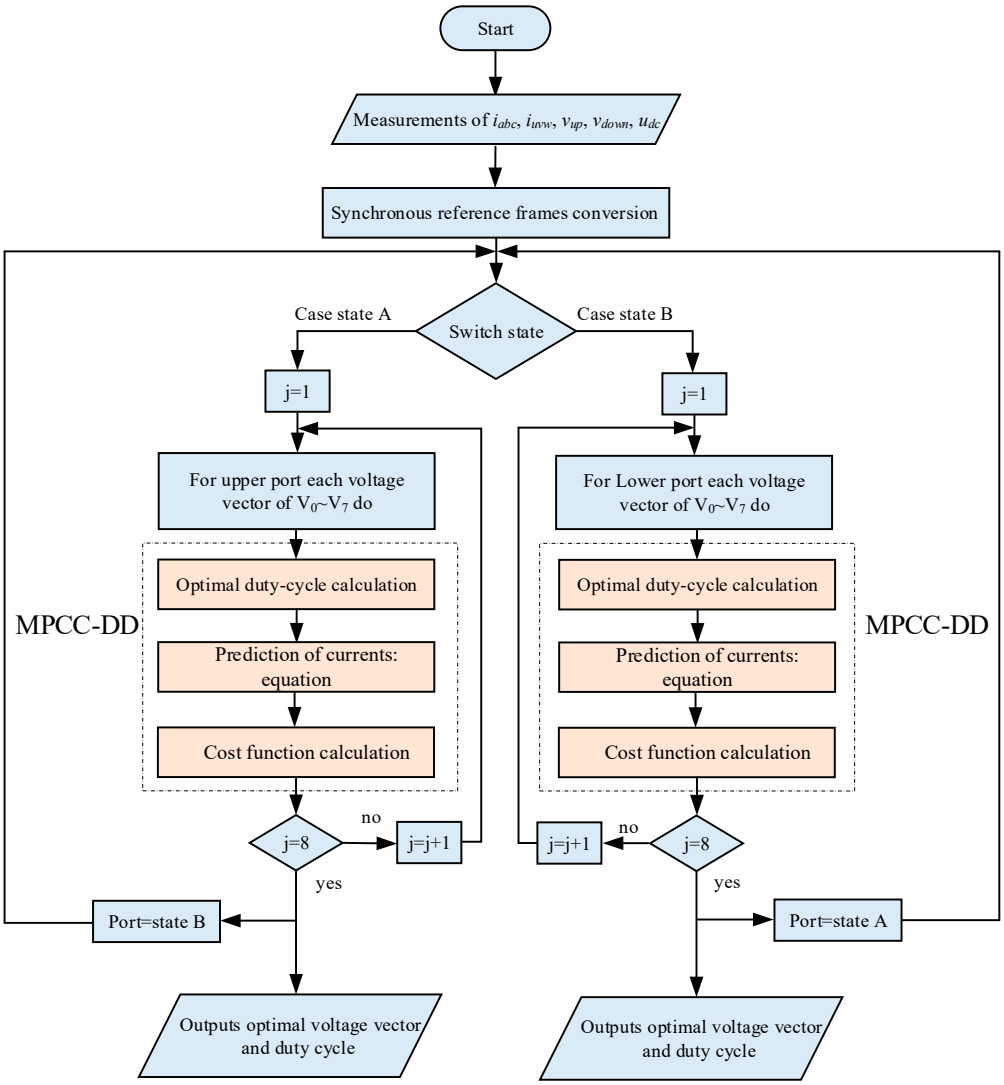

Figure 9. Flowchart of overall control algorithm of MPCC-DD.

5. Simulation Results and Analysis of DP-DDWEPGS

This section introduces the implementation of MPCC-DD under local optimal energy capture. The parameters of the PMLG are as follows (dual translators have the same parameters): L_d = 0.045 H, L_q = 0.045 H, Ψ_f = 5 Wb, τ = 0.1 m. DC load is 120 Ω and DC bus voltage is 200 V.

5.1. Local Optimal Power Capture

According to the sea conditions along the coast of China, the JONSWAP spectrum with a period T of 6.5 s and a significant wave height H_s of 1.75 m is selected [27]. The excitation force on the float from the irregular waves can be obtained. By performing a fast Fourier transform, five main frequencies of the wave excitation force can be identified, with the decomposed parameters listed in Table 1. It is shown in Figure 10 that the fitting excitation force at the selected five main frequencies basically matches the original excitation force and can be a good substitute for it.

Table 1. Main frequency of excitation force.

Frequency (Hz)	Amplitude (N)	Phase (rad)
$f_1 = 0.0333$	876	1.6057
$f_2 = 0.1$	3023	−0.40143
$f_3 = 0.1333$	3541	0.05236
$f_4 = 0.1667$	4009	2.1468
$f_5 = 0.2667$	1098	−0.8203

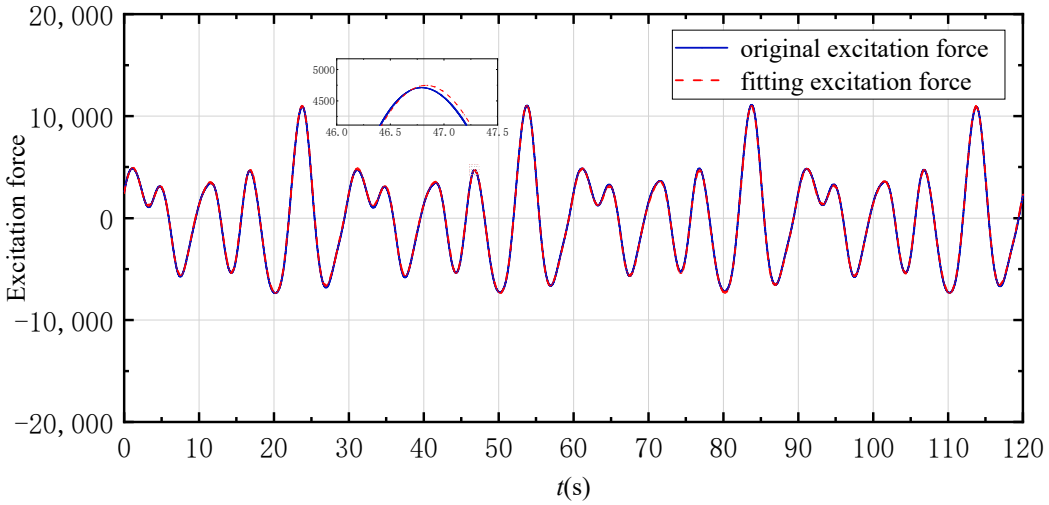

Figure 10. Fitting excitation force and original excitation force.

In practice, it is challenging for the PMLG to accurately track different frequency points simultaneously, and the spring in the DP-DDWEPGS exhibits a delay in adjustment between different frequencies. Therefore, the local optimal power is selected in the paper for further analysis. According to Equations (10) and (12), the power captured by DP-DDWEPGS at a single frequency can be obtained, as shown in formula (29).

$$P_i = \frac{{F_{exi}}^2 R_{pto}}{\left[\omega_i m_\Sigma - \frac{1}{\omega_i}(\rho g S_{float} + k_r + \frac{k_n}{\lambda})\right]^2 + \left[k_{rd} + B_r + \frac{B_n}{\lambda} + R_{pto}\right]^2} \tag{29}$$

where ω_i (i = 1, 2, 3, 4, 5) is the frequency selected from Table 1, F_{exi} is the amplitude of the excitation force corresponding to ω_i, P_i is the power captured by the DP-DDWEPGS with frequency ω_i, $R_{pto} = R_{pto1} + R_{pto2}/\lambda$, $m_\Sigma = m_{add} + m_b + m_1 + m_2/\lambda$.

The power corresponding to each of the five frequencies is calculated through Equation (29), as shown in Figure 11. Each of the five frequencies has its respective optimal damping coefficient, where P_i (i = 1, 2, 3, 4, 5) reaches its maximum value. It can be observed that ω_4 is the frequency with the maximum power in the excitation force.

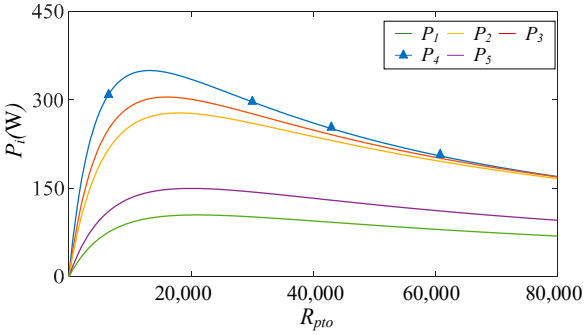

Figure 11. Output power for each frequency.

Meanwhile, the optimal damping coefficient derived from ω_4 allows the system to capture the maximum power, as detailed in Table 2. Therefore, the associated R_{pto} of ω_4 is chosen as the local optimal damping coefficient of the generator for this paper.

Table 2. Total power at five optimal damping coefficients of main frequency of excitation force.

R_{pto}	ΣP_i (i = 1, 2, 3, 4, 5) (W)
21,110 (f_1 = 0.0333)	1162.43
18,003 (f_2 = 0.1)	1168.67
15,911 (f_3 = 0.1333)	1177.58
13,190 (f_4 = 0.1667)	1180.03
20,110 (f_5 = 0.2667)	1166.77

5.2. Comparison of MPCC, MPCC-D, MPCC-DD

Based on the analysis in Section 5.1, the local optimal damping coefficient can be determined. And in Equation (6), the local optimal damping coefficient is used to establish the reference value for the electromagnetic forces of the dual translators under optimal power capture. The electromagnetic force of the PMLG is controlled by the armature current. In this paper, zero d-axis current control is employed, and the electromagnetic force is related to the q-axis current, as described in Equation (15). To match the electromagnetic force with the local optimal damping coefficient, the i_q reference value is calculated through Equation (15). Meanwhile, three control methods are implemented in this paper to control the q-axis current of the PMLG to achieve maximum power capture. Based on the previous analysis, frequency ω_4 of the excitation force has the maximum power. To compare and verify the effectiveness of the controllers, a simulation model based on the excitation force at the frequency ω_4 is established, and comparative simulations are conducted to evaluate the performance of the three controllers. The simulation results are presented in Figure 12.

The q-axis current tracking under MPCC, MPCC-D, and MPCC-DD is shown in Figure 12, where $\Delta i_{q\_up} = i_{q\_upref} - i_{q\_up}$, $\Delta i_{q\_down} = i_{q\_downref} - i_{q\_down}$.

Figure 12a–f show the dual translators' reference and actual currents of the q-axis. Due to the decoupling control of the dual ports, where only one port operates per control cycle, the current ripple in MPCC-D is larger compared to MPCC. Therefore, this paper introduces duty cycle optimization control. As seen in Figure 12c,f, the current ripple in MPCC-DD is significantly reduced. This demonstrates that decomposing a control cycle into the operation of optimal and zero voltage vectors can effectively address the issue of large current ripple in model predictive current control. This improvement is achieved without adding other voltage vectors, meaning that the computational load does not increase significantly.

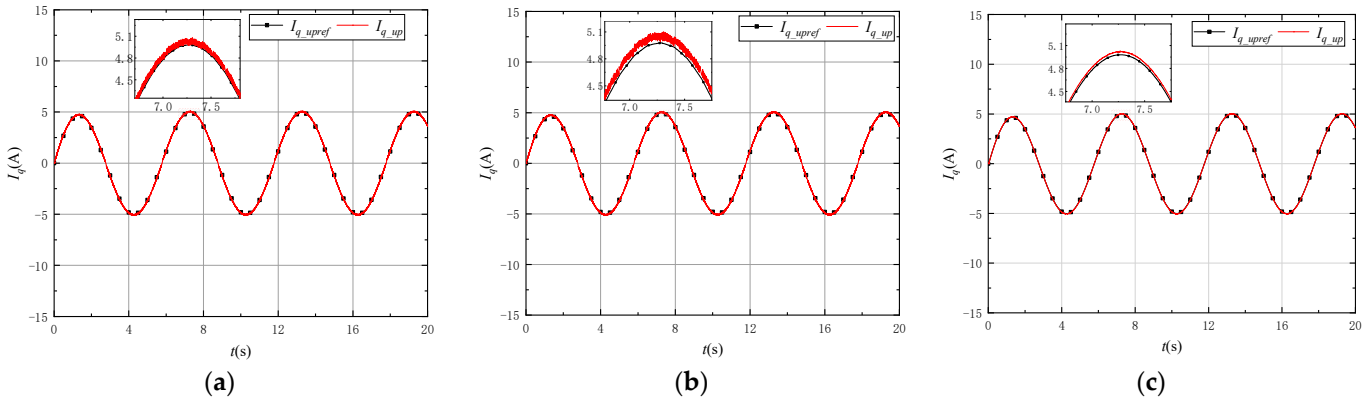

(**a**) (**b**) (**c**)

Figure 12. *Cont.*

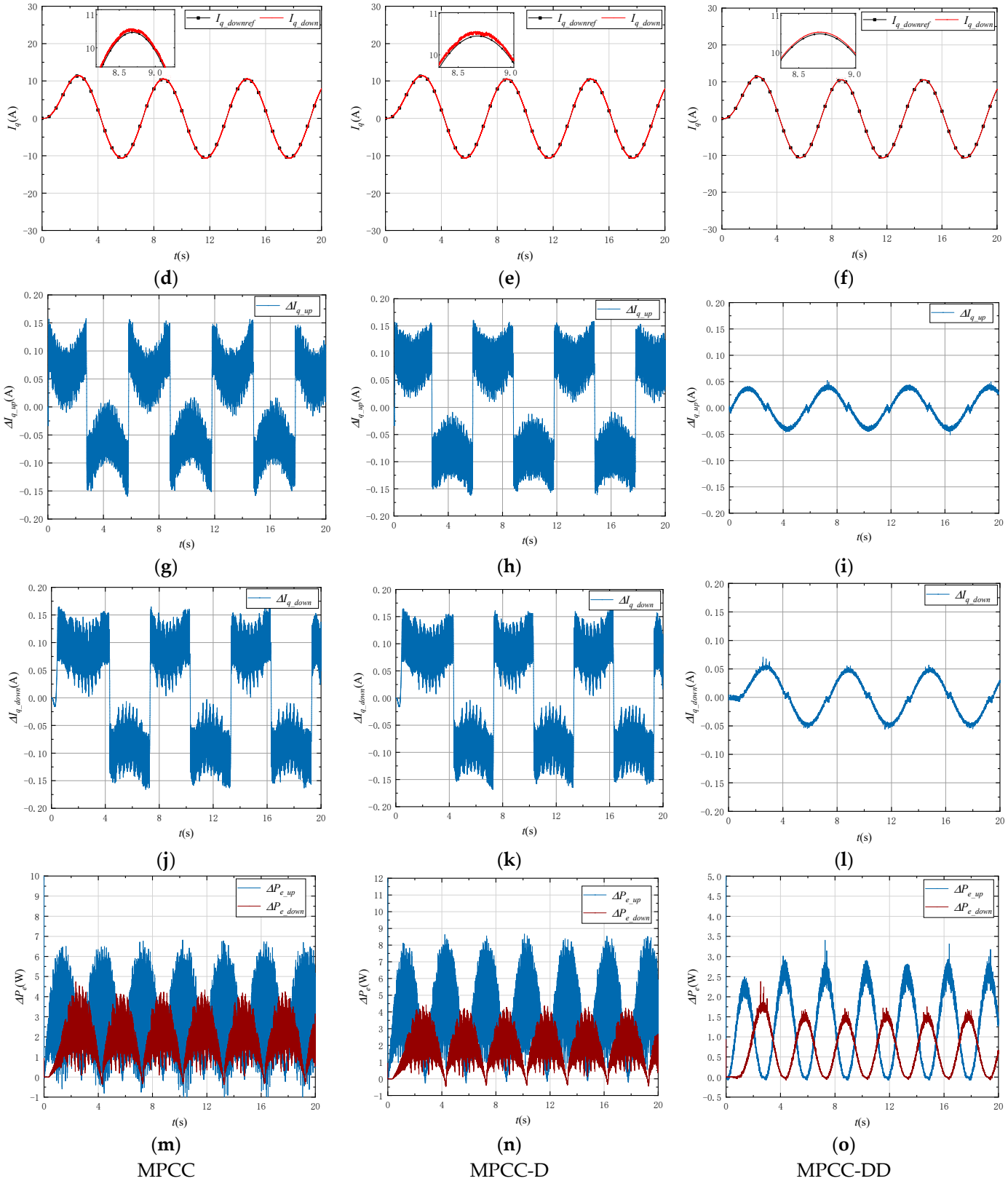

Figure 12. Simulation results under MPCC, MPCC-D, and MPCC-DD. (**a**) i_q of upper translator; (**b**) i_q of dual translator; (**c**) i_q of dual translator; (**d**) i_q of lower translator; (**e**) i_q of lower translator; (**f**) i_q of lower translator; (**g**) Δi_{q_up} of upper translator; (**h**) Δi_{q_up} of upper translator; (**i**) Δi_{q_up} of upper translator; (**j**) Δi_{q_down} of lower translator; (**k**) Δi_{q_down} of lower translator; (**l**) Δi_{q_down} of lower translator; (**m**) Δp_e of dual translator; (**n**) Δp_e of dual translator; (**o**) Δp_e of dual translator.

The differences between the reference and actual currents of the q-axis are shown in Figure 12g–l. These results more intuitively illustrate the advantage of duty cycle optimization in reducing the current ripple. In conventional MPCC, the cost function is the sum of the dual ports' cost functions, as shown in Equations (18) and (19). Consequently, due to the different current magnitudes between the dual ports, the port with the larger current error will dominate the cost function. It is revealed in Figure 12g,j that the current error values for the dual ports are not the same. However, in MPCC-D, the ports are decoupled, and the cost function only reflects the error for the present port under the optimal voltage vector, as shown in Equation (24). Therefore, in MPCC-D, each port selects the optimal voltage vector that minimizes its own error without being influenced by the other port. Consequently, it is shown in Figure 12h,k that the current error values for the dual ports in MPCC-D are nearly identical. And the mutations in Figure 12g,h,j,k result from the velocity commutation of the PMLG translators. Since i_q is proportional to the velocity, at the moment of translator velocity commutation, the value of Δi_q is near its maximum, abruptly changing from positive to negative, thereby causing a mutation. In Figure 12i,l, the commutation mutation is small because the Δi_q value is close to zero at the moment of the translator's velocity commutation.

The error between the theoretical and actual values of power under MPCC, MPCC-D, and MPCC-DD is shown in Figure 12m–o, where $\Delta P_e = P_{e\_ref} - P_e$. In the PMLG used in this paper, $L_d = L_q$, so Equation (14) describes the relationship between i_q and active power. The ripples in active power are primarily caused by that in i_q in the PMLG. In Equation (15), the electromagnetic force of the PMLG is also related to i_q. Under the influence of MPCC-DD, the ripples in i_q are significantly reduced, as shown in Figure 12c,f,i,l. Consequently, the ripples in active power are also greatly reduced, as depicted in Figure 12m–o. This indicates that in MPCC-DD, the active power is much closer to the theoretical value calculated by MPPT, thereby reducing active power loss.

The time required for each main control part of the MPCC, MPCC-D, and MPCC-DD during one execution is shown in Table 3. In the MPCC-D, the control mode is divided into state A and state B, achieving decoupling operation. Decoupling operation only requires the calculation of 8 switching vectors each time, and States A and B alternate during the process, resulting in the computational load of MPCC-D being approximately 20% of that of MPCC. Because of adding the duty cycle optimization, MPCC-DD has a slightly longer operation time than MPCC-D. The switching states of the NSC under MPCC-DD are shown in Figure 13, with state A and state B alternating to achieve decoupling control, accompanied by optimal duty cycle regulation.

Table 3. Time Required for Each Main Control Part Each Cycle.

Control Method	MPCC	MPCC-D	MPCC-DD
Voltage vectors calculations and conversion (10^{-6} s)	18.821	2.836	2.915
Predictions (10^{-6} s)	3.498	0.5	0.563
Cost functions (10^{-6} s)	1.054	0.269	0.274
Duty cycle optimization (10^{-6} s)	—	—	3.078
Else (10^{-6} s)	2.127	1.518	1.775
Total tome(10^{-6} s)	25.5	5.123	8.605

Under the zero d-axis current control strategy, the d-axis current affects the reactive power. The d-axis currents of MPCC and MPCC-DD are shown in Figure 14, and it can be observed that the fluctuation of d-axis currents in MPCC-DD is slightly larger compared with MPCC but remains within the acceptable range. This is because duty cycle control is used in this paper for the q-axis current, which is prioritized in the cost function of Equation (18). However, the simulation results show that MPCC-DD significantly reduces the q-axis current error and ripple, far outweighing the slight increase in the d-axis current error. Moreover, the d-axis current error remains within the acceptable range.

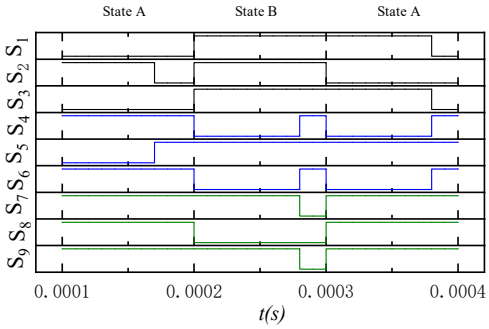

Figure 13. Switching state of the NSC.

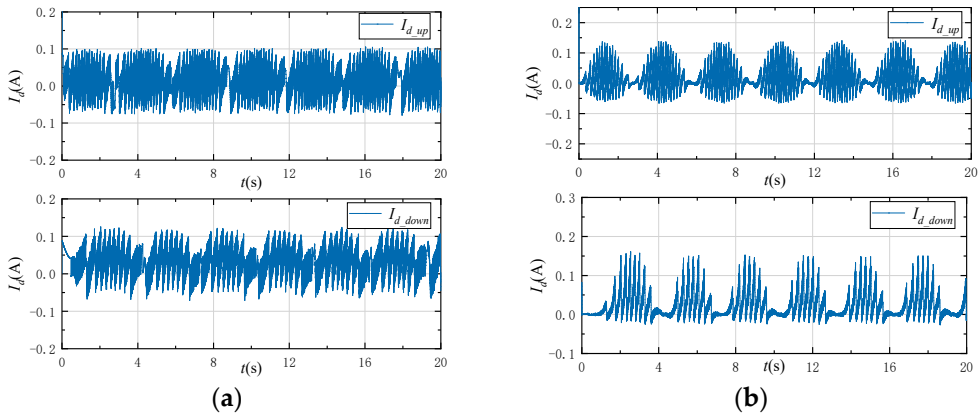

Figure 14. *d*-axis current. (**a**) i_d of dual translator (MPCC); (**b**) i_d of dual translator (MPCC-DD).

5.3. Simulation Analysis of the Control Effect Whole System

To verify the effectiveness of the proposed control method and optimal power capture strategy, a simulation model of the whole system with generators, NSC, and MPC controllers is built. In addition, different control results with regular wave excitation force under optimal frequency and irregular wave excitation force as JONSWAP spectrum are obtained and analyzed.

5.3.1. Simulation of Optimal Frequency Point of Overall System Operation

With regular wave excitation force, the output power of DP-DDWEPGS, the current of HESS, and the DC voltage of NSC are obtained and shown in Figures 15 and 16.

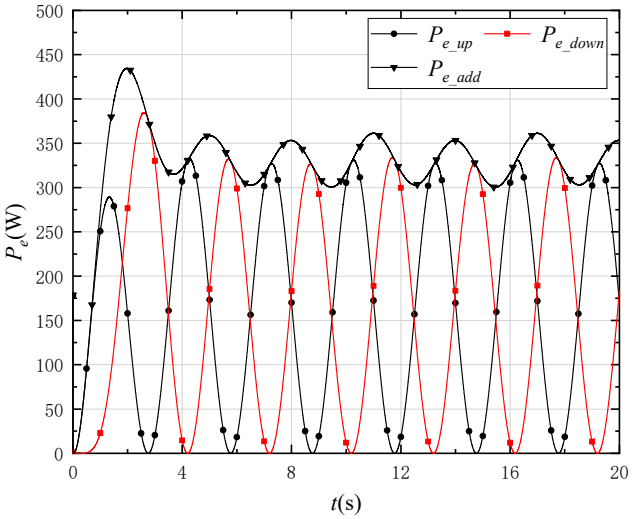

Figure 15. Instantaneous power relationship diagram of dual-translators in DP-DDWEPGS.

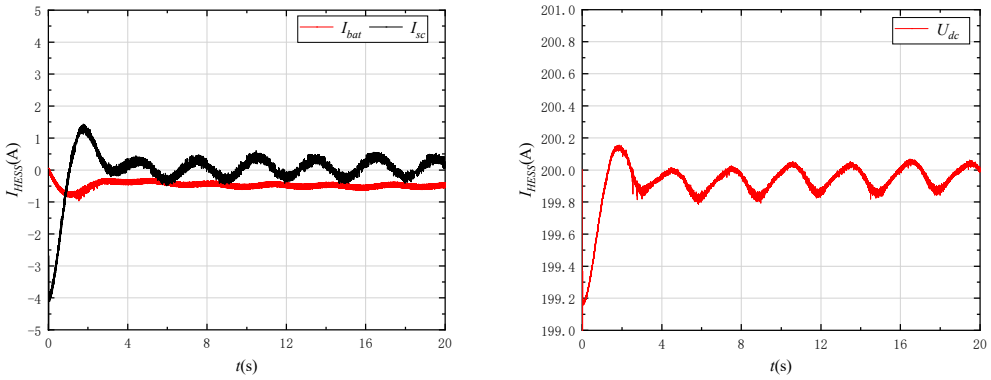

Figure 16. The current and voltage of DC side. (**a**) Current of HESS; (**b**) DC-bus voltage.

As shown in Figure 15. The instantaneous power of the dual translators is complementary, resulting in a smooth, zero-free, and consistent total output instantaneous power, which reduces the impact on the load-side power. Consequently, HESS responds to the high-frequency and low-frequency power with a small amplitude of the response current, as shown in Figure 16a. The supercapacitor suppresses the high-frequency power fluctuation, while the battery suppresses the low-frequency power fluctuation, ensuring that the DC bus voltage is stabilized at a given value. As shown in Figure 16b, the steady-state fluctuation of the DC voltage is 0.2 V, indicating that the system performs well.

5.3.2. Operation Results of DP-DDWEPGS in Irregular Waves

Under the irregular wave excitation force of the JONSWAP spectrum, the generator damping factor of the upper and lower translator is controlled to achieve full complementarity and the optimal damping coefficient under optimal frequency ω_4, as shown in Figure 11. And the simulation results are obtained and shown in Figures 17–19. Firstly, as the current i_q is used to control the electromagnetic force of generators and implement damping control, the different currents $i_{q,}$ under different frequency wave excitation force obtained by Fourier decomposition from the JONSWAP spectrum are implemented in the system and are controlled by using the MPCC-DD controller using the duty cycle control method. The simulation results are obtained and shown in Figure 17.

It can be seen that by using the MPCC-DD controller with the duty cycle control method, the q-axis current under different frequencies can be controlled to follow the reference value well and achieve target damping.

Moreover, an irregular wave excitation with JONSWAP spectrum performance is implemented during system operation. The d-axis current, q-axis current of the upper port, speed of the translator, and output power of the upper and lower power port, respectively, are obtained by using the proposed MPCC-DD controller using the duty cycle control method. The simulation results are shown in Figures 18 and 19.

As we can see, due to the action of irregular waves, the magnitude and frequency of the translator velocity are constantly changing, and the frequency and magnitude of i_q can be found through Equation (15), which also varies with the velocity. The d/q current of the upper and lower power ports can be controlled with a small bias between input and feedback values. This indicates that the proposed controller has the advantages of quick following and good broadband frequency response performance and is suitable for wave power generation systems with variable frequency input power. However, it can be seen that at maximum transient power (about 24 s), the lower d current increases because it is the highest speed and force point, and the angular error also increases. Therefore, to obtain a more perfect performance, instantaneous high speed and force should be considered.

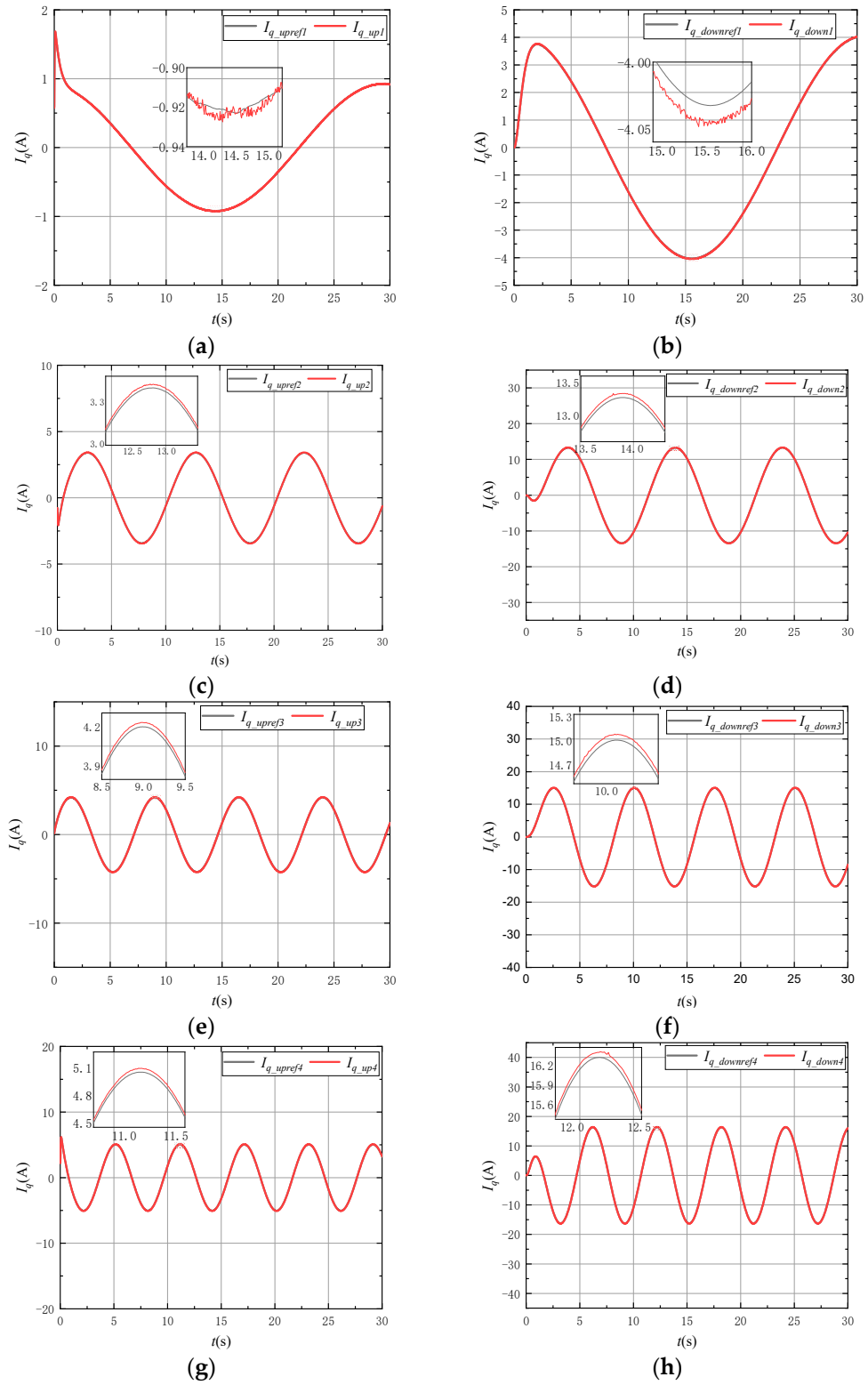

Figure 17. *Cont.*

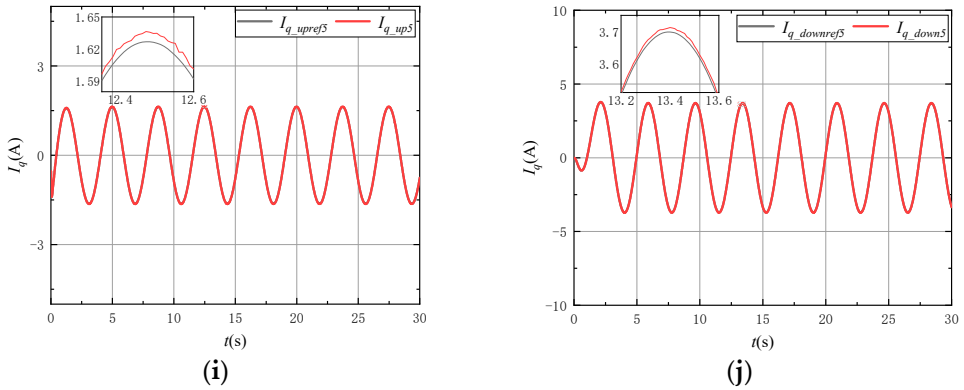

Figure 17. The simulation effect of control of q-axis current under different frequencies. (**a**) i_q of upper power port under frequency f_1; (**b**) i_q of lower power port under frequency f_1; (**c**) i_q of upper power port under frequency f_2; (**d**) i_q of lower power port under frequency f_2; (**e**) i_q of upper power port under frequency f_3; (**f**) i_q of lower power port under frequency f_3; (**g**) i_q of upper power port under frequency f_4; (**h**) i_q of lower power port under frequency f_4; (**i**) i_q of upper power port under frequency f_5; (**j**) i_q of lower power port under frequency f_5.

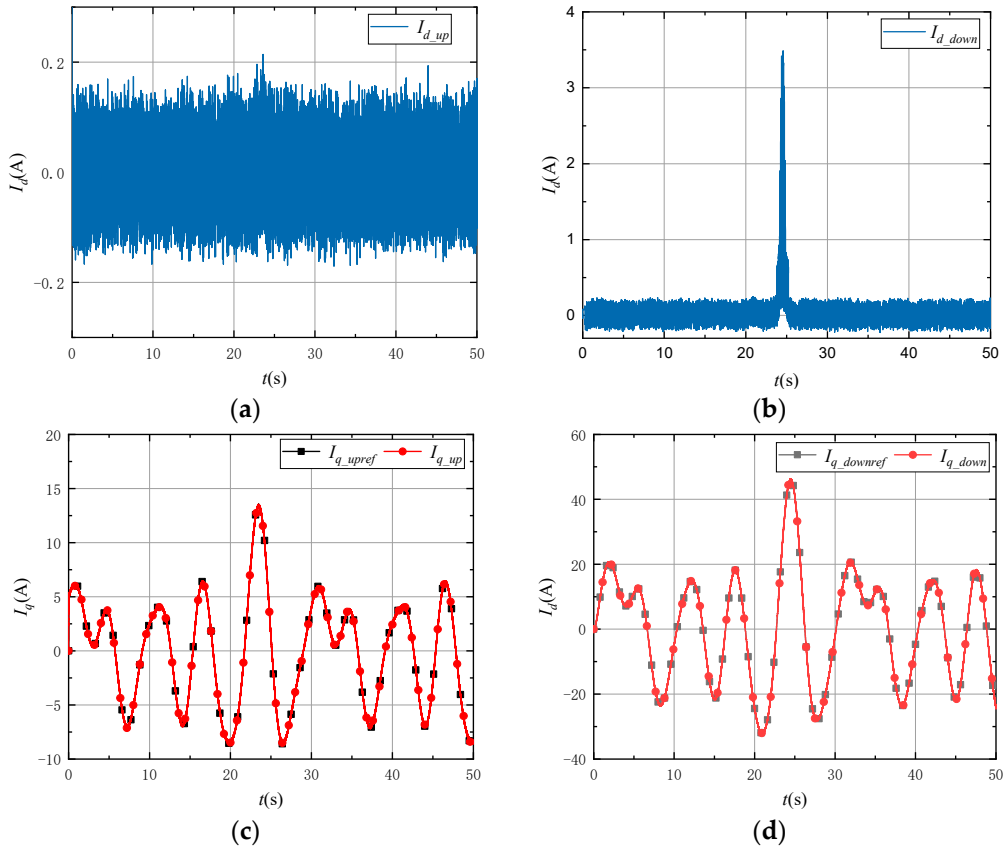

Figure 18. The d/q current of generators under irregular wave excitation. (**a**) i_d of upper under irregular wave excitation; (**b**) i_d of lower under irregular wave excitation; (**c**) i_q of upper under irregular wave excitation; (**d**) i_q of lower under irregular wave excitation.

Figure 19 shows the speed, output power, and actual damping of the upper and lower power ports.

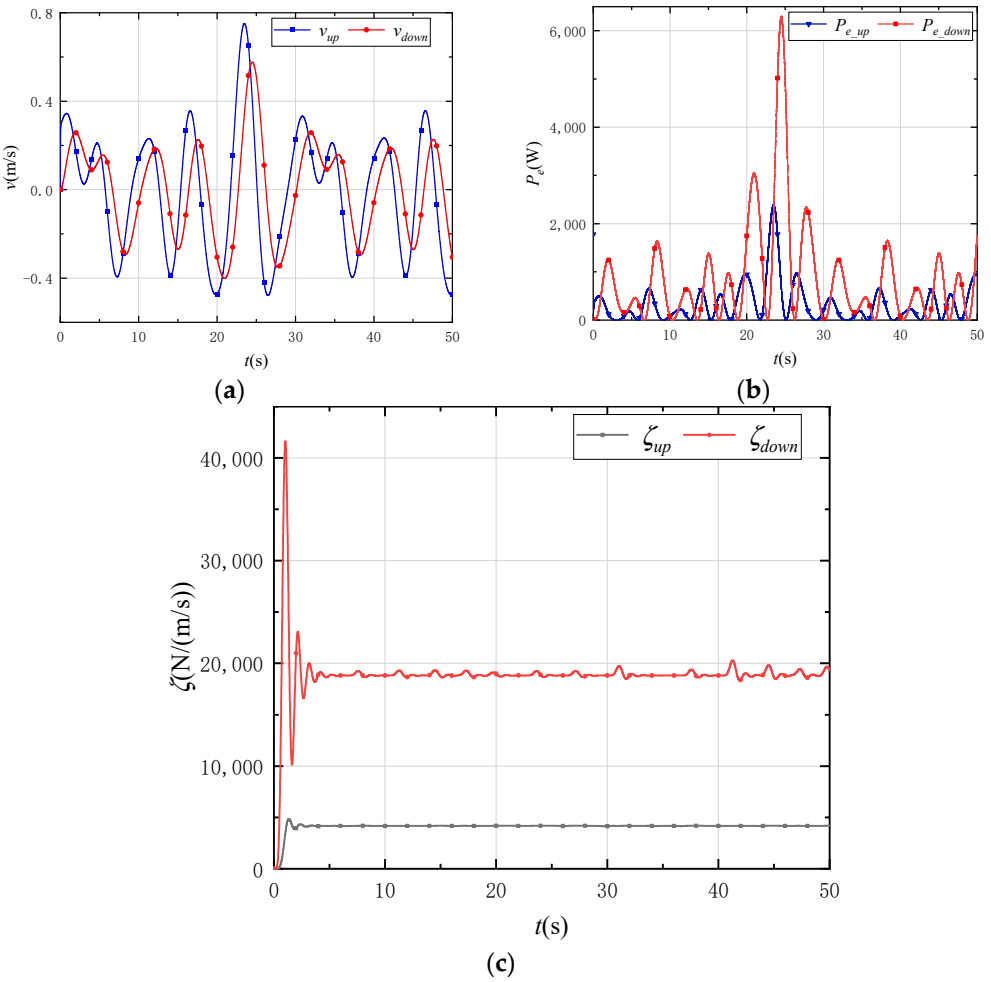

Figure 19. Performance of system under irregular waves. (**a**) Speed of upper and lower power port; (**b**) Dynamic power of upper and lower power port; (**c**) Damping of upper and lower power port.

From the controlled damping, it can be seen that the damping has very small fluctuations, a well-controlled effect. In addition, the spring coefficient is fixed, due to the use of a mechanical spring between the dual translators. The spring coefficient is determined based on the excitation force corresponding to ω_4, which contains the maximum power. The irregular waves consist of multiple frequency components, as shown in Table 1, the output powers of the dual translators are no longer completely complementary under irregular wave conditions. Nevertheless, compared with conventional SP-DDWEPGS, it is observed in Figure 19 that the overall power fluctuations of the DP-DDWEPGS are reduced, and the power complementarity effect still works.

6. Conclusions

In this paper, the equivalent circuit diagram of DP-DDWEPGS is first constructed to implement the optimal power capture control. Then, a multiport converter for DP-DDWEPGS is proposed by employing switch multiplexing, which reduces the number of switching devices and lowers the failure rate and cost compared to conventional three-phase VSR and bidirectional DC-DC converters. By dividing the NSC into two operating states, the NSC decouples the control of its dual ports. Compared to conventional MPCC, the computation time of MPCC-D is reduced by 80%. However, because the MPCC-D applies a voltage vector only once per control cycle and operates with only one port at a time, it results in high current ripples and errors. Therefore, duty cycle optimization is performed using the deadbeat control principle, significantly reducing current ripples and errors. This reduction leads to decreased electromagnetic force ripples in the PMLG, bringing the

output power closer to the theoretical value produced by MPPT. Simulation results prove the feasibility of optimal power capture control and reveal that the ripples are effectively reduced in PMLG current and active power. This is achieved with a computational burden still smaller than that of conventional MPCC.

Author Contributions: Methodology, L.H.; Software, J.Z.; Validation, S.W. (Shiquan Wu); Investigation, B.P.; Data curation, H.L.; Writing—original draft, S.W. (Shixiang Wang). All authors have read and agreed to the published version of the manuscript.

Funding: This research was funded by National Natural Science Foundation of China, grant number 41876096.

Institutional Review Board Statement: Not applicable.

Informed Consent Statement: Not applicable.

Data Availability Statement: The original contributions presented in the study are included in the article, further inquiries can be directed to the corresponding author.

Conflicts of Interest: The authors declare no conflict of interest.

Appendix A

Table A1. NSC possible switching states and dual ports voltage vectors.

Switching States [S_1–S_9]	Upper Port Voltage Vector	Lower Port Voltage Vector
[111111000]	V_7 (0)	V_7 (0)
[110111001]	V_2 ($2/3U_{dc}e^{j\pi/3}$)	V_2 ($2/3U_{dc}e^{j\pi/3}$)
[111110001]	V_7 (0)	V_2 ($2/3U_{dc}e^{j\pi/3}$)
[101111010]	V_6 ($2/3U_{dc}e^{j5\pi/3}$)	V_6 ($2/3U_{dc}e^{j5\pi/3}$)
[100111011]	V_1 ($2/3U_{dc}e^{j0}$)	V_1 ($2/3U_{dc}e^{j0}$)
[101110011]	V_6 ($2/3U_{dc}e^{j5\pi/3}$)	V_1 ($2/3U_{dc}e^{j0}$)
[111101010]	V_7 (0)	V_6 ($2/3U_{dc}e^{j5\pi/3}$)
[110101011]	V_2 ($2/3U_{dc}e^{j\pi/3}$)	V_1 ($2/3U_{dc}e^{j0}$)
[111100011]	V_7 (0)	V_1 ($2/3U_{dc}e^{j0}$)
[011111100]	V_4 ($2/3U_{dc}e^{j\pi}$)	V_4 ($2/3U_{dc}e^{j\pi}$)
[010111101]	V_3 ($2/3U_{dc}e^{j2\pi/3}$)	V_3 ($2/3U_{dc}e^{j2\pi/3}$)
[011110101]	V_4 ($2/3U_{dc}e^{j\pi}$)	V_3 ($2/3U_{dc}e^{j2\pi/3}$)
[001111110]	V_5 ($2/3U_{dc}e^{j4\pi/3}$)	V_5 ($2/3U_{dc}e^{j4\pi/3}$)
[000111111]	V_0 (0)	V_0 (0)
[001110111]	V_5 ($2/3U_{dc}e^{j4\pi/3}$)	V_0 (0)
[011101110]	V_4 ($2/3U_{dc}e^{j\pi}$)	V_5 ($2/3U_{dc}e^{j4\pi/3}$)
[010101111]	V_3 ($2/3U_{dc}e^{j2\pi/3}$)	V_0 (0)
[011100111]	V_4 ($2/3U_{dc}e^{j\pi}$)	V_0 (0)
[111011100]	V_7 (0)	V_4 ($2/3U_{dc}e^{j\pi}$)
[110011101]	V_2 ($2/3U_{dc}e^{j\pi/3}$)	V_3 ($2/3U_{dc}e^{j2\pi/3}$)
[111010101]	V_7 (0)	V_3 ($2/3U_{dc}e^{j2\pi/3}$)
[101011110]	V_6 ($2/3U_{dc}e^{j5\pi/3}$)	V_5 ($2/3U_{dc}e^{j4\pi/3}$)
[100011111]	V_1 ($2/3U_{dc}e^{j0}$)	V_0 (0)
[101010111]	V_6 ($2/3U_{dc}e^{j5\pi/3}$)	V_0 (0)
[111001110]	V_7 (0)	V_5 ($2/3U_{dc}e^{j4\pi/3}$)
[110001111]	V_2 ($2/3U_{dc}e^{j\pi/3}$)	V_0 (0)
[111000111]	V_7 (0)	V_0 (0)

Table A2. Acronyms.

Acronyms	Full Form
DP-DDWEPGS	dual-port direct drive wave energy power generation system
SP-DDWEPGS	single-port direct drive wave energy power generation system
FCS-MPC	finite control set model predictive control
DDWEPGS	direct drive wave energy power generation system
PMLG	permanent magnet linear generator
VSR	voltage source rectifier
HESS	hybrid energy storage system
NSC	nine-switch converter
MPCC	model predictive current control
MPCC-D	decoupling model predictive current control
MPCC-DD	decoupling duty cycle optimization model predictive current control

References

1. Xiao, X.; Huang, X.; Kang, Q. A Hill-Climbing-Method-Based Maximum-Power-Point-Tracking Strategy for Direct-Drive Wave Energy Converters. *IEEE Trans. Ind. Electron.* **2016**, *63*, 257–267. [CrossRef]
2. Sun, Z.G.; Cheung, N.C.; Zhao, S.W.; Lu, Y.; Shi, Z.H. Design and simulation of a linear switched reluctance generator for wave energy conversion. In Proceedings of the 2011 4th International Conference on Power Electronics Systems and Applications, Hong Kong, China, 11 August 2011; pp. 1–5.
3. Farrok, O.; Islam, M.R.; Muttaqi, K.M.; Sutanto, D.; Zhu, J. Design and Optimization of a Novel Dual-Port Linear Generator for Oceanic Wave Energy Conversion. *IEEE Trans. Ind. Electron.* **2020**, *67*, 3409–3418. [CrossRef]
4. Rasool, S.; Islam, M.R.; Muttaqi, K.M.; Sutanto, D. Coupled Modeling and Advanced Control for Smooth Operation of a Grid-Connected Linear Electric Generator Based Wave-to-Wire System. *IEEE Trans. Ind. Appl.* **2020**, *56*, 5575–5584. [CrossRef]
5. Liu, H.; Huang, L.; Li, Y.; Yang, J.; Zhang, J. Resonance control to eliminate reactive power of an improved dual-port direct-drive wave energy converter. *Ocean Eng.* **2023**, *288*, 116007. [CrossRef]
6. Wu, H.; Xu, P.; Hu, H.; Zhou, Z.; Xing, Y. Multiport Converters Based on Integration of Full-Bridge and Bidirectional DC-DC Topologies for Renewable Generation Systems. *IEEE Trans. Ind. Electron.* **2014**, *61*, 856–869. [CrossRef]
7. Jarutus, N.; Kumsuwan, Y. A Carrier-Based Phase-Shift Space Vector Modulation Strategy for a Nine-Switch Inverter. *IEEE Trans. Power Electron.* **2017**, *32*, 3425–3441. [CrossRef]
8. Liu, X.; Loh, P.C.; Wang, P.; Blaabjerg, F. A Direct Power Conversion Topology for Grid Integration of Hybrid AC/DC Energy Resources. *IEEE Trans. Ind. Electron.* **2013**, *60*, 5696–5707. [CrossRef]
9. Gao, F.; Zhang, L.; Li, D.; Loh, P.C.; Tang, Y.; Gao, H. Optimal Pulsewidth Modulation of Nine-Switch Converter. *IEEE Trans. Power Electron.* **2010**, *25*, 2331–2343. [CrossRef]
10. Pan, L.; Zhang, J.; Zhang, J.; Pang, Y.; Wang, B.; Wang, K.; Xu, D. A Novel Space-Vector Modulation Method for Nine-Switch Converter. *IEEE Trans. Power Electron.* **2020**, *35*, 1789–1804. [CrossRef]
11. de Andrade, F.C.; Bradaschia, F.; Limongi, L.R.; Cavalcanti, M.C. A Reduced Switching Loss Technique Based on Generalized Scalar PWM for Nine-Switch Inverters. *IEEE Trans. Ind. Electron.* **2018**, *65*, 38–48. [CrossRef]
12. Abdel-Moneim, M.G.; Abdel-Azim, W.E.; Abdel-Khalik, A.S.; Hamed, M.S.; Ahmed, S. Model Predictive Current Control of Nine-Switch Inverter-Fed Six-Phase Induction Motor Drives Under Healthy and Fault Scenarios. *IEEE Trans. Transp. Electrif.* **2024**. [CrossRef]
13. Lee, S.S.; Heng, Y.E.; Roslan, M.A. Finite control set model predictive control of nine-switch AC/DC/AC converter. In Proceedings of the 2016 IEEE International Conference on Power and Energy (PECon), Melaka, Malaysia, 28–29 November 2016; pp. 746–751.
14. Kouro, S.; Cortes, P.; Vargas, R.; Ammann, U.; Rodriguez, J. Model Predictive Control—A Simple and Powerful Method to Control Power Converters. *IEEE Trans. Ind. Electron.* **2009**, *56*, 1826–1838. [CrossRef]
15. Gao, H.; Wu, B.; Xu, D. Nine-switch ac/ac current source converter for microgrid application with model predictive control. *IET Power Electron.* **2017**, *10*, 1759–1766. [CrossRef]
16. Gulbudak, O.; Santi, E. Model predictive control of dual-output nine-switch inverter with output filter. In Proceedings of the 2015 IEEE Energy Conversion Congress and Exposition (ECCE), Montreal, QC, Canada, 20–24 September 2015; pp. 1582–1589. [CrossRef]
17. Guazzelli, P.R.U.; Castro, A.G.D.; Dos Santos, S.T.C.A.; de Oliveira, C.M.R.; Pereira, W.C.A.; Monteiro, J.R.B.A.; Aguiar, M.L.D. Dual Predictive Current Control of Grid Connected Nine-Switch Converter Applied to Induction Generator. In Proceedings of the 2018 13th IEEE International Conference on Industry Applications (INDUSCON), Sao Paulo, Brazil, 12–14 November 2018; pp. 1038–1044.
18. Aciego, J.J.; Gonzalez Prieto, I.; Duran, M.J.; Bermudez, M.; Salas-Biedma, P. Model Predictive Control Based on Dynamic Voltage Vectors for Six-Phase Induction Machines. *IEEE J. Emerg. Sel. Top. Power Electron.* **2021**, *9*, 2710–2722. [CrossRef]
19. Zhang, Y.; Xie, W.; Li, Z.; Zhang, Y. Model Predictive Direct Power Control of a PWM Rectifier With Duty Cycle Optimization. *IEEE Trans. Power Electron.* **2013**, *28*, 5343–5351. [CrossRef]

20. Nikzad, M.R.; Asaei, B.; Ahmadi, S.O. Discrete Duty-Cycle-Control Method for Direct Torque Control of Induction Motor Drives With Model Predictive Solution. *IEEE Trans. Power Electron.* **2018**, *33*, 2317–2329. [CrossRef]
21. Nie, Z.; Xiao, X.; Yi, H.; Kang, Q. Direct drive wave energy converters integrated with a composite energy storage system. In Proceedings of the 2011 International Conference on Electrical Machines and Systems, Beijing, China, 20–23 August 2011; pp. 1–5.
22. Manandhar, U.; Ukil, A.; Gooi, H.B.; Tummuru, N.R.; Kollimalla, S.K.; Wang, B.; Chaudhari, K. Energy Management and Control for Grid Connected Hybrid Energy Storage System Under Different Operating Modes. *IEEE Trans. Smart Grid* **2019**, *10*, 1626–1636. [CrossRef]
23. Copping, A.; Battey, H.; Brown-Saracino, J.; Massaua, M.; Smith, C. An international assessment of the environmental effects of marine energy development. *Ocean. Coast. Manag.* **2014**, *99*, 3–13. [CrossRef]
24. Dong, J.; Chen, G.; Deng, Y.; Wang, K.; He, X. A family of integrated dual-output DC-DC converters: Synthesis methodology and performance analysis. In Proceedings of the 2016 IEEE 8th International Power Electronics and Motion Control Conference (IPEMC-ECCE Asia), Hefei, China, 22–26 May 2016; pp. 342–347.
25. O'Sullivan, A.C.M.; Lightbody, G. Co-design of a wave energy converter using constrained predictive control. *Renew. Energy* **2017**, *102*, 142–156. [CrossRef]
26. Manandhar, U.; Tummuru, N.R.; Kollimalla, S.K.; Ukil, A.; Beng, G.H.; Chaudhari, K. Validation of Faster Joint Control Strategy for Battery- and Supercapacitor-Based Energy Storage System. *IEEE Trans. Ind. Electron.* **2018**, *65*, 3286–3295. [CrossRef]
27. Wu, S.; Liu, C.; Chen, X. Offshore wave energy resource assessment in the East China Sea. *Renew. Energy* **2015**, *76*, 628–636. [CrossRef]